energies

MDPI

Article

Output Impedance Control Method of Inverter-Based Distributed Generators for Autonomous Microgrid †

Youn-Ok Choi and Jaehong Kim *

Department of Electrical Engineering, Chosun University, 309, Pilmun-daero, Dong-gu, Gwangju 61452, Korea; yochoi@chosun.ac.kr

* Correspondence: jaehong77@gmail.com; Tel.: +82-10-8220-5665

† This paper is an extended version of our paper published in Proceedings of the 2016 IEEE 8th International Power Electronics and Motion Control Conference (IPEMC), Hefei, China, 22–25 May 2016.

Received: 25 May 2017 ; Accepted: 28 June 2017 ; Published: 2 July 2017

Abstract: The droop method is the most favorable alternative in microgrid implementations for autonomous control of grid-forming inverter-based distributed generators (DGs) connected in parallel. However, the dynamic characteristic of the conventional droop method is poor because the inertias of inverter-based DG units are extremely low and the transmission line is normally very short. An output impedance control method to enhance the dynamic performance and minimize the circulating current between grid-forming DGs is devised in this study. It is shown that it also enhances the power and harmonic sharing accuracy. The proposed method utilizes the virtual output impedance as a control signal for reactive power flow management. The effectiveness of the proposed scheme is validated using the high-speed field programmable gate array (FPGA)-based real-time hardware-in-the-loop test results.

Keywords: inverters; microgrid; droop control; distributed generators (DGs); uninterruptable power supply (UPS)

1. Introduction

Increasing use of renewable energy resources (RESs) in the utility power grid has led to the increasing utilization of inverter-based distributed generators (DGs) [1]. The increasing number of inverter-based DGs requires new strategies for the operation of the local power grid in order to maintain the reliability and quality of power-supply [2]. In order to achieve better operation of multiple inverter-based DG units, the microgrid concept has been well accepted [3–5].

The microgrid can operate in both grid-connected and intentional islanding modes for the reliable power supply to local loads. Owing to its good expendability and wireless nature, the autonomous configuration of islanding microgrid is well accepted. The droop method has been the most favorable alternative among the existing well-known autonomous control methods [3,4,6,7]. The droop method does not have a critical high bandwidth communication link between the DG units because it uses only local information. However, the conventional droop method has several drawbacks, such as a high dependency on the inverter output impedance, a trade-off between voltage deviation and power-sharing accuracy, a slow transient response, and unbalanced harmonic current sharing [8,9]. As a result, the islanding microgrid may have power quality problems owing to extremely low inertia, the increased presence of non-linear loads, etc. [6].

Various types of modified droop methods have been developed in order to enhance the dynamic performance of the conventional droop method [10]. To reduce the reactive power sharing error, a virtual output impedance concept was devised in [7] and a voltage restoration method was utilized in [11]. To enhance the power sharing performance, an improved droop control method, which utilizes voltage measurement at the point of common coupling (PCC), was proposed in [12]. To improve the harmonic sharing performance between the droop-controlled DG units. a cooperative harmonic filtering strategy was introduced in [13]. To prevent an unstable operation of the islanding microgrid, the concepts of virtual frequency and virtual voltage magnitude were proposed in [14].

A virtual impedance concept cooperating was introduced in [7]. This simple and effective output impedance control method has been adopted in recent studies to improve the stability, load sharing performance, and power quality of a microgrid [6,15]. Although virtual impedance is considered to be a promising method it has not been a main controller but an ancillary control mean [16].

In this study, a part of the droop control is replaced by the virtual impedance control. The performance of the proposed method is compared with that of the conventional control. The performance comparison is implemented using a field programmable gate array (FPGA)-based high-speed real-time hardware-in-the-loop (HIL) test, which describes almost all the fast electrical events in power electronic devices.

2. System Model

The circuit topology of an inverter-based microgrid which n-DG units feed local loads is shown in Figure 1. DG units have two types of power electronic converters. One is the bi-directional DC/DC converter, which converts low DC voltage supplied from its own distributed energy resource (DER) to high DC link voltage. Another is the DC/AC inverter, which supplies high quality AC power to the local AC bus. DG units are connected to the local AC bus with feeder impedances, r_{ox} and L_{ox}, where the subscript x is in $[1, n]$. Further, L_{fx}, C_{fx}, and Z_L denote the filter inductance, filter capacitance, and local load impedance of x-th DG unit, respectively. Thus, the inverter in a DG unit is connected to the local AC bus via an inductor-capacitor-inductor (LCL) type intermediate impedance.

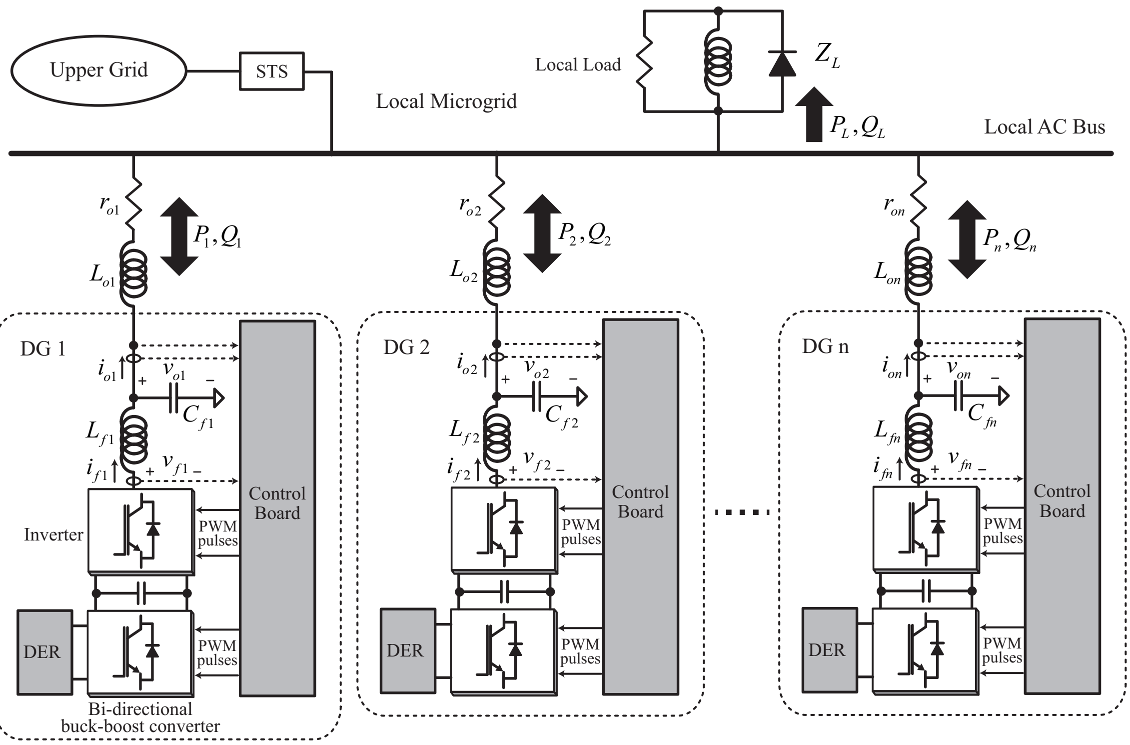

Figure 1. System configuration of inverter-based microgrid.

A microgrid has two operation modes, grid-connected mode and islanding mode. In the grid-connected mode, the static transfer switch (STS) is turned on and the upper grid is connected to a local microgrid. Every DG unit in the local microgrid supplies active current (real power) to the local AC bus in-phase with the grid voltage [17]. Thus, in this case, each DG unit controls the outlet current i_{ox} flowing through r_{ox} and L_{ox}. When a fault occurs in the upper grid or the total amount of local power generation exceeds the local power demand, the STS is switched off and the local microgrid enters the intentional islanding mode [18]. In this case, the DG units control the output filter capacitor voltage v_{oi} to collaboratively form the local bus voltage and maintain appropriate load sharing with other DG units based on their own generation capacity.

2.1. Power Flow Model in Islanding Microgrid

In the islanding mode, DG units participate in feeding the local loads by controlling the capacitor voltage, v_{ox}. The reference value v_{ox}^* is generated by a front power controller such as the droop or virtual synchronous machine (VSM) method [19]. When the capacitor voltage v_{ox} is controlled properly, the inverter with the LC filter in Figure 1 is considered as an ideal voltage source with its own internal impedance Z_{ox} as shown in Figure 2. Z_{ox} is highly dependent on the control of the inverter at each DG unit. The equivalent circuit shown in Figure 2 is a case wherein two DG units are connected in parallel, but this equivalent circuit is directly expanded to every case with an arbitrary number of DG units connected in parallel.

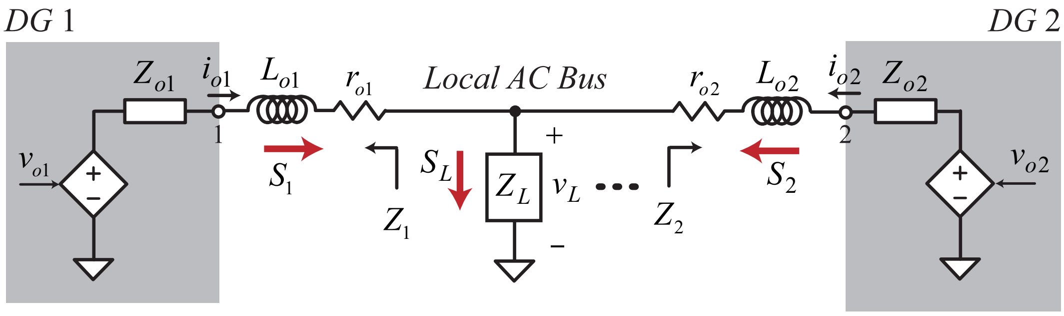

Figure 2. Equivalent circuit diagram of inverter-based microgrid.

Assume the following phasor notation: $v_{o1} = |v_{o1}|e^{j\theta_{o1}}$, $v_{o2} = |v_{o2}|e^{j\theta_{o2}}$, $v_L = |v_L|e^{j\theta_L}$, and $Z_1 = |Z_1|e^{j\angle Z_1}$. The power transmission equation from DG unit 1 to the local AC bus is derived from Figure 2 as

$$\begin{aligned} S_1 &= v_{o1} i_{o1}^* \\ &= \frac{|v_{o1}|^2}{|Z_1|} e^{j\angle Z_1} - \frac{|v_{o1}||v_L|}{|Z_1|} e^{j(\angle Z_1 + \theta_{1L})}, \end{aligned} \tag{1}$$

where $\theta_{1L} = \theta_{o1} - \theta_L$ and $Z_1 = Z_{o1} + \omega_L L_{o1} e^{\frac{\pi}{2}} + r_{o1}$ [20]. Subsequently, the real and reactive power transmission from DG unit 1 to the local AC bus is derived from (1) as

$$P_1 = Re\{S_1\} = \left(\frac{|v_{o1}|^2}{|Z_1|} - \frac{|v_{o1}||v_L|}{|Z_1|} \cos\theta_{1L} \right) \cos\angle Z_1 + \frac{|v_{o1}||v_L|}{|Z_1|} \sin\theta_{1L} \sin\angle Z_1, \tag{2}$$

$$Q_1 = Im\{S_1\} = \left(\frac{|v_{o1}|^2}{|Z_1|} - \frac{|v_{o1}||v_L|}{|Z_1|} \cos\theta_{1L} \right) \sin\angle Z_1 - \frac{|v_{o1}||v_L|}{|Z_1|} \sin\theta_{1L} \cos\angle Z_1. \tag{3}$$

Similarly, the real and reactive power transmission from DG unit 1 to DG unit 2 is calculated as

$$P_{12} = \left(\frac{|v_{o1}|^2}{|Z_{12}|} - \frac{|v_{o1}||v_{o2}|}{|Z_{12}|} \cos\theta_{12} \right) \cos\angle Z_{12} + \frac{|v_{o1}||v_{o2}|}{|Z_{12}|} \sin\theta_{12} \sin\angle Z_{12}, \tag{4}$$

$$Q_{12} = \left(\frac{|v_{o1}|^2}{|Z_{12}|} - \frac{|v_{o1}||v_{o2}|}{|Z_{12}|} \cos\theta_{12} \right) \sin\angle Z_{12} - \frac{|v_{o1}||v_{o2}|}{|Z_{12}|} \sin\theta_{12} \cos\angle Z_{12}, \tag{5}$$

where $\theta_{12} = \theta_{o1} - \theta_{o2}$, $Z_{12} = Z_1 + Z_2$. It can be observed from Equations (2) and (3) that the real and reactive power transmission is determined not only by the magnitude and phase difference of the generator voltage, but also by the magnitude and phase of the intermediate impedance. There are two objectives in this study. The first objective is to minimize Equations (4) and (5), which are the real and reactive power transmission between the generators. The power transmission between the DG units provokes power oscillations in the local microgrid and eventually causes system failure. The other objective is to enhance the load sharing performance characterized by Equations (2) and (3).

2.2. Implementation of the Virtual Output Impedance

The internal impedance values of DG unit 1 and DG unit 2, i.e., Z_{o1} and Z_{o2}, in Figure 2 can be adjusted by the control software. It is called the virtual impedance concept [7,9]. The virtual impedance Z_{vx} in x-th DG unit is emulated by subtracting the calculated instantaneous voltage drop from the voltage reference v_{ox}^* as shown in Figure 3, i.e.,

$$\begin{aligned} v_x^* &= v_{ox}^* - v_{vx} \\ &= v_{ox}^* - Z_{vx} i_{ox}. \end{aligned} \tag{6}$$

In practice, Z_{ox} is highly affected by the voltage control performance in terms of the voltage control bandwidth, overshoot, and rising time [21]. However, if the voltage control bandwidth is very wide compared with the grid frequency, an inverter with the LC filter can be considered as an ideal voltage source near the grid frequency [9]. Subsequently, the internal impedance Z_{ox} approximately becomes Z_{vx} as shown in Figure 3.

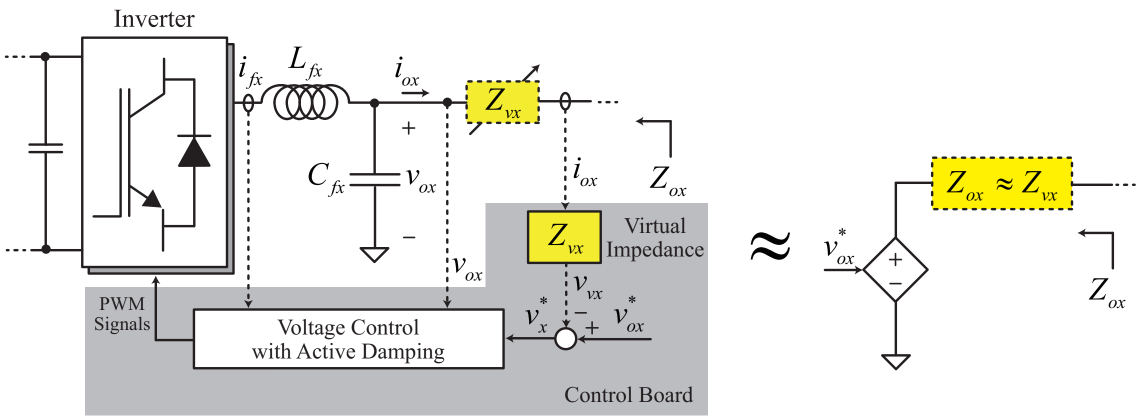

Figure 3. Equivalent circuit diagram of inverter-based microgrid.

In order to emulate the inductive impedance, in the Laplace domain, Z_{vx} should be

$$Z_{vx}(s) = sL_{vx}, \tag{7}$$

where s and L_{vx} are the Laplace operator and the inductance value to be virtually emulated, respectively. Thus, the virtual voltage drop in the virtual inductor is calculated as

$$v_{vx}(s) = sL_{vx} i_{ox}(s). \tag{8}$$

Notably, a derivative of i_{ox} is required in Equation (8). However, for practical implementation, $v_{vx}(s)/i_{ox}(s)$ should be proper. A first order low-pass filter (LPF) can be added to make Equation (8) a proper transfer function as

$$v_{vx}(s) = L_{vx} \frac{\omega_v s}{s + \omega_v} i_{ox}(s), \tag{9}$$

where ω_v is the cut-off frequency of the first order LPF. It can be observed from Equation (9) that L_{vx} is a band-limited inductance, which is effective only in the low frequency region below ω_v. The value of the virtual inductance is normally a few millihenry or less for a stable parallel operation between the voltage-controlled DG units, and, subsequently, sL_{vx} becomes a dominant impedance in Z_{ox}, i.e.,

$$Z_{ox} \approx Z_{vx} = sL_{vx}. \tag{10}$$

A complex z-domain representation of Equation (9) for the digital software implementation is calculated by utilizing the bilinear approximation, $s \approx (2 - 2z^{-1})/(T + Tz^{-1})$, as

$$v_{vx}(z) = L_{vx} \frac{2\omega_v - 2\omega_v z^{-1}}{(\omega_v T_s + 2) + (\omega_v T_s - 2)z^{-1}} i_{ox}(z), \tag{11}$$

where z and T_s are the z-transform operator and sampling time, respectively.

2.3. Principle of Conventional Droop Control

The droop control method was developed based on the analysis of steady-state power flow in an inductive feeder [6,22]. The conventional frequency and voltage magnitude droop controllers are

$$\omega_{ox}^* = \omega_n + D_{px}(\overline{P}_x - P_x), \tag{12}$$
$$|v_{ox}|^* = V_n + D_{qx}(\overline{Q}_x - Q_x), \tag{13}$$

where ω_n, V_n, D_{px}, and D_{qx} are the nominal angular frequency, nominal voltage magnitude, P-ω droop gain, and Q-V droop gain of x-th DG unit, respectively. $\overline{P}_x$ and $\overline{Q}_x$ are the nominal real and reactive power ratings of the DG unit x, respectively. The instantaneous reference voltage v_{ox}^* is obtained using Equations (12) and (13), i.e., $v_{ox}^* = |v_{ox}|^* \cos \omega_{ox}^* t$. A strict limitation in the frequency and magnitude variation $\omega_{ox}^* = (1 \pm 1.0\%)\omega_n$ and $|v_{ox}|^* = (1 \pm 5\%)V_n$ is applied to avoid any desynchronization between the islanding DG units [23]. The reference voltage v_{ox}^* is always sinusoidal with little distortion.

3. Active Impedance Control Method for Minimum Circulating Current and Enhanced Power Sharing Performance

3.1. Power Flow Analysis of the Conventional Droop Control

Using the virtual impedance method, the intermediate impedance Z_x can be effectively more inductive, i.e.,

$$\begin{aligned} Z_x &= r_{ox} + 2\pi f_n L_{ox} e^{j\frac{\pi}{2}} + Z_{ox} \\ &\approx r_{ox} + 2\pi f_n (L_{ox} + L_{vx}) e^{j\frac{\pi}{2}}, \end{aligned} \tag{14}$$

where f_n is the nominal frequency of the grid voltage. Therefore, $\angle Z = tan^{-1}((100\pi(L_{ox} + L_{vx}))/r_{ox})$ at 50 Hz grid system. As L_{vx} becomes larger, the phase angle of Z_x becomes closer to $\pi/2$,

On the other hand, in the conventional droop method, P-ω and Q-V droop control equations are derived from the power flow characteristics in the pure inductive intermediate impedance condition. It can be observed from Equations (12) and (13) that the conventional droop method adjusts the phase angle and magnitude of output voltage reference to control the real and reactive power transmission, respectively. From the power Equations (2) and (3), the power transmission characteristics, with respect to the values of intermediate resistance and inductance, are shown in Figures 4 and 5. The phase angles of the DG output voltage and the local bus voltage are the same and only the magnitudes are different in Figure 4. In an ideal case, $r_{o1} = 0$, i.e., the real power flow between DG unit 1 and the local AC bus should be zero because Equation (2) becomes zero when $\theta_{1L} = 0$ and $\angle Z_1 = \pi/2$. However, practically, the feeder resistance is not zero and as r_{o1} becomes larger, a considerable amount of real power is transmitted to the local AC bus in Figure 4a. Notably, the feeder inductance is normally over 0.5 mH.

It is also observed that undesirable real power flow decreases gradually as the virtual inductance value becomes larger. On the other hand, the amount of reactive power transmission converges to 1 kVar in the large inductance region in Figure 4b.

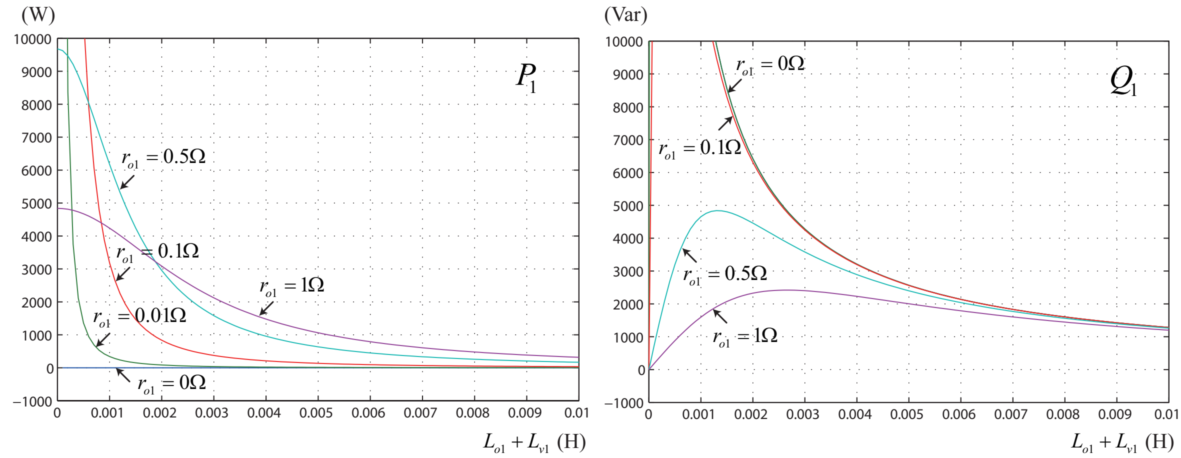

(**a**) (**b**)

Figure 4. Power flow variation with respect to the inductance values when $\angle v_{o1} = \angle v_L$ and $|v_{o1}| = 1.05|v_L|$: (**a**) real power flow; (**b**) reactive power flow.

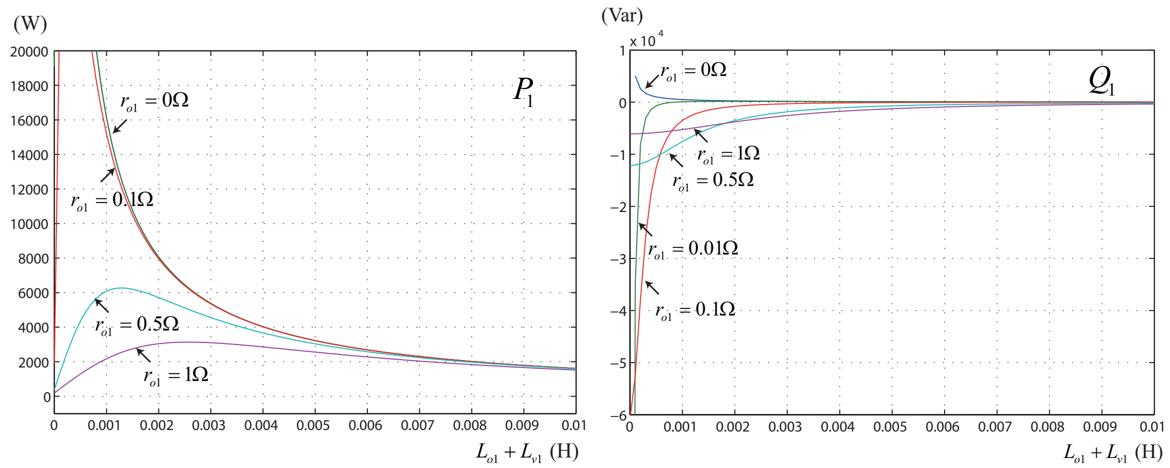

(**a**) (**b**)

Figure 5. Power flow variation with respect to the inductance values when $|v_{o1}| = |v_L|$ and $\angle v_{o1} = \angle v_L + 0.005\pi$: (**a**) real power flow; (**b**) reactive power flow.

Similar power transmission characteristics, but in reverse, are observed in Figure 5. In this case, the magnitudes are the same and the phase angles are slightly different at each side. The reactive power flow from DG unit 1 to the local AC bus is zero in the ideal case, i.e., $r_{o1} = 0$, because Equation (3) becomes zero when $|v_{o1}| = |v_L|$ and $\angle Z_1 = \pi/2$. As long as r_{o1} is not ideally zero, more undesirable reactive power is transmitted to the local AC bus as r_{o1} becomes larger. However, as the virtual inductance value increases, the amount of reactive power transmission settles down to zero.

Consequently, if the intermediate inductance is sufficiently large, i.e., larger than 8 mH, the effect of r_{o1} is almost removed. This is an important advantage of the virtual inductance. It can be expected from Figures 4 and 5 that the use of the virtual inductance enhances the power transmission accuracy in the voltage-controlled DG units.

If the intermediate impedance is almost purely inductive with the virtual inductance, the real and reactive power transmission equations, Equations (2) and (3), can be reasonably approximated to

$$P_1 \approx \frac{|v_{o1}||v_L|}{\omega_n L_1}\sin\theta_{1L}, \tag{15}$$

$$Q_1 \approx \frac{|v_{o1}|^2}{\omega_n L_1} - \frac{|v_{o1}||v_L|}{\omega_n L_1}\cos\theta_{1L}, \tag{16}$$

where $L_1 = L_{v1} + L_{o1}$. Similarly, the real and reactive power transmission from DG unit 2 to the local AC bus is

$$P_2 \approx \frac{|v_{o2}||v_L|}{\omega_n L_2}\sin\theta_{2L}, \tag{17}$$

$$Q_2 \approx \frac{|v_{o2}|^2}{\omega_n L_2} - \frac{|v_{o2}||v_L|}{\omega_n L_2}\cos\theta_{2L}, \tag{18}$$

where $L_2 = L_{v2} + L_{o2}$. Equations (4) and (5) can be approximated to

$$P_{12} \approx \frac{|v_{o1}||v_{o2}|}{\omega_n L_{12}}\sin\theta_{12}, \tag{19}$$

$$Q_{12} \approx \frac{|v_{o1}|^2}{\omega_n L_{12}} - \frac{|v_{o1}||v_{o2}|}{\omega_n L_{12}}\cos\theta_{12}, \tag{20}$$

where $L_{12} = L_1 + L_2$. It can be observed from Figures 4 and 5 that approximations Equations (15)–(20) are practically reasonable only when the intermediate inductances L_1 and L_2 are large. The intermediate inductances can be effectively enlarged with the virtual inductance in the low frequency region. Note that the virtual inductance is a band-limited inductance.

3.2. Control Strategy for Minimum Circulating Current: Active Impedance Control Method

In order to minimize the reactive power transmission between DG units 1 and 2, the magnitude of Equation (20) should be minimized, i.e., $Q_{12} = -Q_{21} = 0$, while maintaining the appropriate real and reactive power share characterized by Equations (15)–(18). A possible solution is to equate the magnitudes of the output voltage, i.e., $|V_{o1}| = |V_{o2}|$. This is the main idea of this study. Notably, in the conventional droop control, the dynamic behavior of the reactive power transmission is controlled by the magnitude of the LC filter output voltage as shown in Equation (13). Furthermore, θ_{12} is normally very small and $\cos\theta_{12}$ is very close to 1 [20].

Since L_{v1} and L_{v2} are controllable, L_1 and L_2 are also controllable. Subsequently, we can utilize L_1 and L_2 for the reactive power control instead of utilizing the Q-V droop. With the constraint $|V_{o1}| = |V_{o2}|$, the real power sharing ratio P_2/P_1 is determined from Equation (15) and Equation (17) as

$$\left.\frac{P_2}{P_1}\right|_{|v_{o1}|=|v_{o2}|=V_n} \approx \frac{\sin\theta_{2L}}{\sin\theta_{1L}} \times \frac{L_1}{L_2}. \tag{21}$$

Since θ_{1L} and θ_{2L} are normally very small, Equation (21) can be simplified with the small-signal approximation method as

$$\left.\frac{P_2}{P_1}\right|_{|v_{o1}|=|v_{o2}|=V_n} \approx \frac{\theta_{2L}}{\theta_{1L}} \times \frac{L_1}{L_2}. \tag{22}$$

It can be observed from Label (22) that the real power sharing ratio is determined not only by the angle difference but also by the output inductance ratio.

On the other hand, the reactive power sharing ratio is determined by Equations (16) and (18) as

$$\left.\frac{Q_2}{Q_1}\right|_{|v_{o1}|=|v_{o2}|=V_n} \approx \frac{(V_n - |v_L|) + |v_L|(1-\cos\theta_{1L})}{(V_n - |v_L|) + |v_L|(1-\cos\theta_{2L})} \times \frac{L_1}{L_2}. \tag{23}$$

Since θ_{1L} and θ_{2L} are very small, Equation (23) can be further simplified as

$$\frac{Q_2}{Q_1}\Big|_{|v_{o1}|=|v_{o2}|=V_n} = \frac{a_2}{a_1} \approx \frac{L_1}{L_2}, \tag{24}$$

where a_1 and a_2 are the power sharing ratios of DG unit 1 and DG unit 2, i.e., $a_1 + a_2 + \cdots + a_n = 1$. Equation (24) shows the direct relationship between the reactive power and output inductance value. The reactive power sharing ratio is inversely proportional to the output inductance ratio.

Since the virtual inductance value is controllable, it is utilized as a control variable in this study. Let L_n be a nominal inductance, whose value is the same for all the DG units in the steady-state. For a proper reactive power sharing, from Equation (24), L_n in the x-th DG unit should be

$$L_n = a_x L_x = a_x(L_{vx} + L_{ox}). \tag{25}$$

L_n is a known constant in all DG units, i.e., $L_n = 1$ mH and $a_1L_1 = a_2L_2 = \ldots = a_nL_n$. Therefore, for appropriate reactive power sharing, the virtual inductance value L_{vx} is determined based on the power sharing ratio of the x-th DG unit as

$$L_{vx} = \frac{L_n}{a_x} - L_{ox}. \tag{26}$$

The subsequent step is to compensate the coupling term in the real power control. The real power transmission is also affected by the output inductance ratio in Equation (22). Control decoupling is achieved by modifying the P-ω droop characteristic. The real power transmission is linearly proportional to the phase angle difference and inversely proportional to the total output inductance in Equation (22). Therefore, the conventional P-ω droop control Equation (12) is modified to

$$\omega_x^* = \omega_n + m_x\frac{L_x}{L_n}(\overline{P}_x - P_x), \tag{27}$$

where m_x is the P-ω droop gain. Since the DG units do not communicate with each other (autonomous operation), standard setpoints are required for the power controls. ω_n, V_n, and L_n are the standard setpoint values and they are 314.159 rad/s, 311.127 V, and 0.001 H, respectively, in this study. The phase-locked-loop (PLL) estimates θ_x for the synchronization with the local AC bus voltage in real-time. The resultant overall control block diagram is depicted in Figure 6.

3.3. Stability Analysis

Equivalent block diagrams of the proposed real and reactive power control derived from Figure 6b are shown in Figure 7. V_x denotes the nominal magnitude of the local AC bus voltage. V_x is assumed to vary slowly because the power control bandwidth is very narrow. T_v denotes the transfer function of the voltage control loop and the proportional-integral (PI) control is utilized to regulate the output capacitor voltage, i.e., $G_v = k_p + k_i/s$. Therefore, from Figure 6b, T_v is calculated as

$$T_v = \frac{k_p r_{Cx} C_{fx} s^2 + (k_p + k_i r_{Cx} C_{fx})s + k_i}{L_{fx}C_{fx}s^3 + C_{fx}(r_{Lx} + r_d + r_{Cx} + k_p r_{Cx})s^2 + (1 + k_p + k_i r_{Cx} C_{fx})s + k_i}, \tag{28}$$

where r_d is the virtual resistance of the active damping control [24].

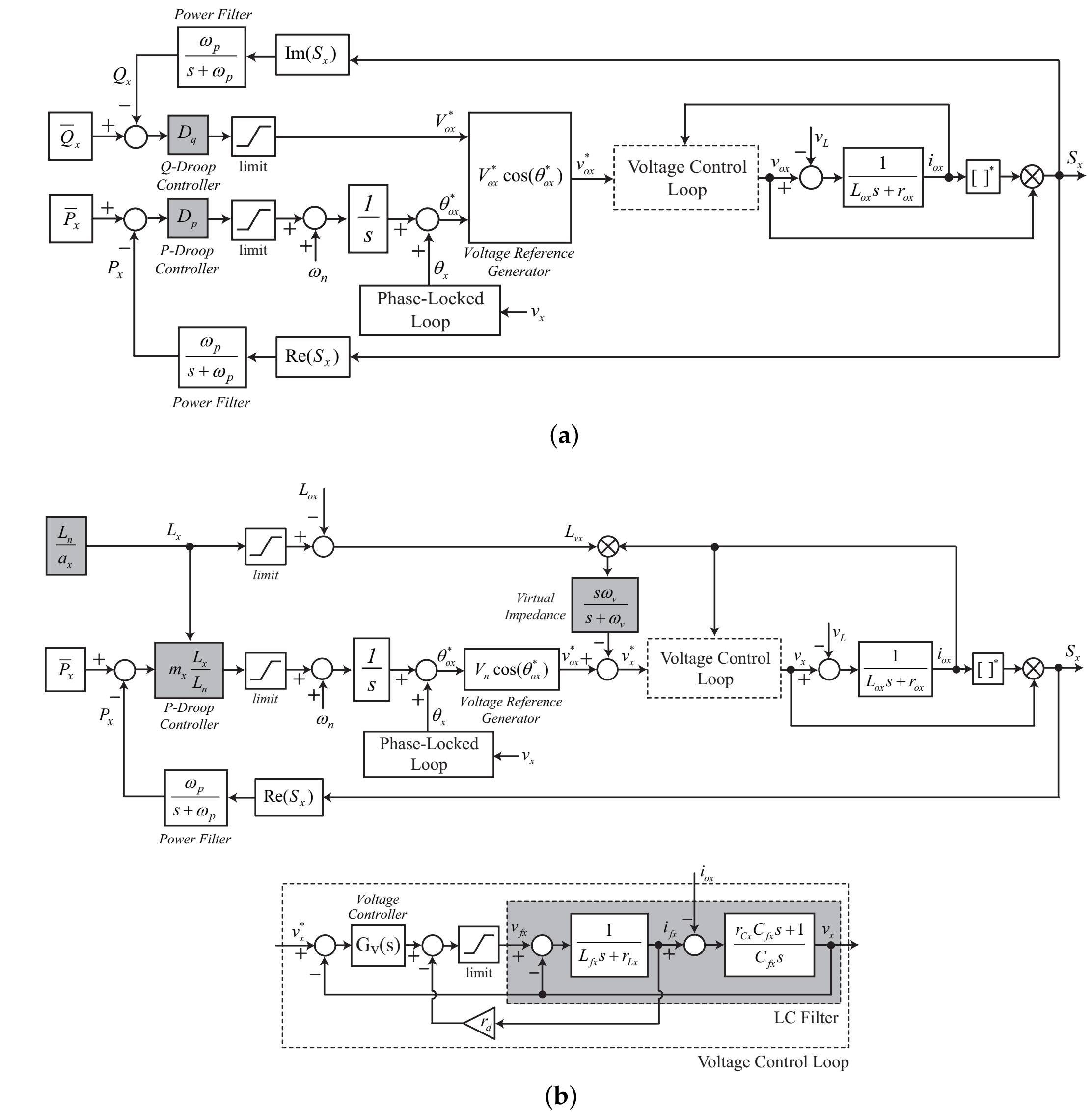

Figure 6. Overall control block diagram: (**a**) conventional droop method; (**b**) proposed active impedance control.

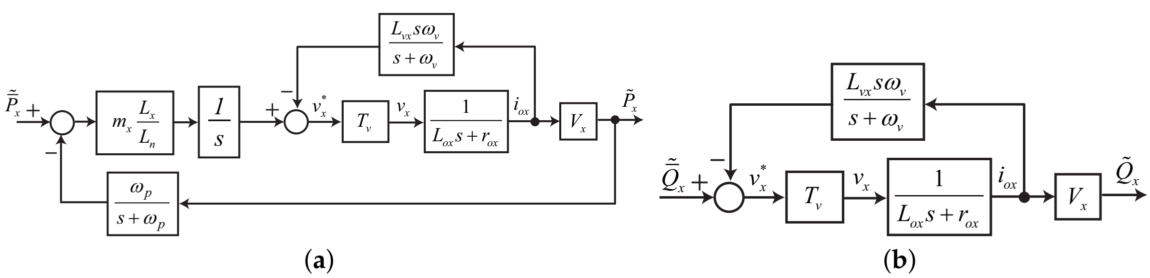

Figure 7. Equivalent block diagram of Figure 6: (**a**) real power control; (**b**) reactive power control.

The real power control transfer function is derived from Figure 7a as

$$\frac{\tilde{P}_x}{\tilde{\bar{P}}_x} = \frac{A(s+\omega_p)}{s + A\omega_p + \omega_p}, \tag{29}$$

where

$$A = \frac{m_x V_x L_x T_v (s + \omega_v)}{L_n L_{ox} s^3 + L_n (L_{ox}\omega_v + r_{ox} + T_v L_{vx}\omega_v) s^2 + L_n r_{ox}\omega_v s}. \tag{30}$$

On the other hand, the reactive power control transfer function is derived from Figure 7b as

$$\frac{\tilde{Q}_x}{\tilde{\tilde{Q}}_x} = \frac{V_x T_v (s + \omega_v)}{L_{ox} s^2 + (L_{ox}\omega_v + r_{ox} + T_v L_{vx}\omega_v) s + r_{ox}\omega_v s}. \tag{31}$$

Pole-zero locations of transfer functions, Equations (29) and (31), are shown in Figure 8 and system poles are listed in Table 1. Note that large virtual inductance values induce conjugate pole pairs on the imaginary axis and thus they provoke oscillations in the controlled power output. Therefore, L_{vx} can not exceed 20 mH. This is a limitation of the proposed control method.

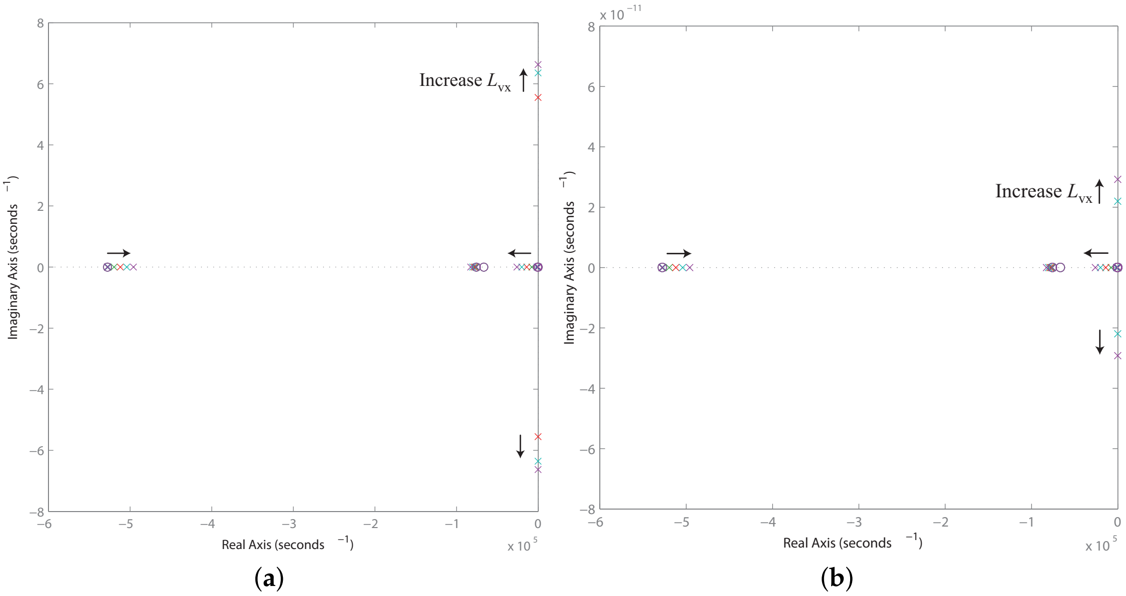

Figure 8. Pole-zero locations: (**a**) real power control; (**b**) reactive power control.

Table 1. Exact pole locations.

L_{vx} (mH)	Poles of $\tilde{P}_x/\tilde{\tilde{P}}_x$
1	−527,770, −527,040, −75,930, −75,830, −1360, −90, −60, 0, 0, 0
11	−527,770, −519,610, −77,090, −75,830, −7710, −60, −10, 0, 0, 0
21	−527,770, −511,960, −78,520, −75,830, −13,950, −60, 0, 0, 5.33 j, −5.33 j
31	−527,770, −504,050, −80,310, −75,830, −20,060, −60, 0, 0, 6.32 j, −6.32 j
41	−527,770, −495,870, −82,590, −75,830, −25,970, −60, 0, 0, 6.65 j, −6.65 j
L_{vx} (mH)	**Poles of $\tilde{Q}_x/\tilde{\tilde{Q}}_x$**
1	−527,770, −527,040, −75,930, −75,830, −1360, −90, 0, 0
11	−527,770, −519,610, −77,090, −75,830, −7710, −20, 0, 0
21	−527,770, −511,960, −78,520, −75,830, −13,950, −10, 0, 0
31	−527,770, −504,050, −80,310, −75,830, −20,060, −10, 2.25×10^{-9} j, -2.25×10^{-9} j
41	−527,770, −495,870, −82,590, −75,830, −25,970, 0, 2.87×10^{-9} j, -2.87×10^{-9} j

4. FPGA Based Real-Time HIL Test Result

In order to validate the effectiveness of the active impedance control method, an FPGA-based real-time (RT) HIL system was built. OPAL-RT's OP4500 HIL system (Montreal, QC, Canada) with a ML605 signal processing board was utilized [25]. Two inverter-based DG unit models and local load models are connected in parallel to form a local electrical power system (EPS). Each DG unit model is composed of a single-phase full-bridge inverter for the DC-to-AC power conversion and a bi-directional buck-boost converter with DC power storage. Power electronic device and circuit models are run in the FPGA, Xilinx Virtex-6 (San Jose, CA, USA), once every 500 ns. The proposed control algorithm is run in one of 6-CPUs and the control frequency is 10 kHz. Pulse-width-modulation (PWM) pulses from the CPU are captured (time-stamped) and the exact pulse-width is transferred to the FPGA in real time. The generation capacity of DG unit 1 is set to 20 kW, whereas that of DG unit 2 is set to 10 kW. The detailed parameters are listed in Table 2.

Table 2. System & control parameters.

Parameter	DG Unit 1	DG Unit 2	Parameter	DG Unit 1	DG Unit 2
L_{ox}, (mH)	0.01	0.03	r_{ox}, (Ω)	0.1	0.2
L_{fx}, (mH)	1	1	C_{fx}, (μF)	50	50
r_{Lx}, (Ω)	0.25	0.25	r_{Cx}, (Ω)	0.4	0.4
L_n, (mH)	1	1	f_n, (Hz)	50	50
$\overline{P}$, (kW)	20	10	$\overline{Q}$, (kVar)	20	10
m_x	0.000157	0.000314	ω_v	628.32	628.32
r_d, (Ω)	3	3	a_x	0.66	0.33
k_{pv}	0.6	0.6	k_{iv}	2000	2000

The load sharing performances in pure resistive and pure inductive load conditions are compared in Figure 9. It is shown that the real and reactive power share is not proportional to the generation capacity using the conventional droop method in Figure 9a. Notably, the generation capacity of DG unit 1 is two times larger than that of DG unit 2. Furthermore, considerable phase mismatches between i_{o1} and i_{o2} are observed in Figure 9a. The phase mismatch in the pure resistive load condition represents undesirable reactive power transmission between DG units 1 and 2 and the phase mismatch in the pure inductive load condition represents undesirable real power transmission between DG units 1 and 2. Owing to poor power sharing accuracy and the coupled characteristic of the conventional droop method, a considerable amount of real and reactive circulating current flows between the DG units. Moreover, the generators with different power ratings connected in parallel use different droop gains. Different droop gains result in a difference between the voltage references of the two grid-forming DG units, which are the power control outputs. This electrical potential difference between v_{o1} and v_{o2} in Figure 2 causes the power transmission between DG units 1 and 2.

On the other hand, the magnitude of the voltage references in every DG unit is fixed using the proposed method. Thus, there is no reactive current flow between the DG units in an ideal case. The resultant current waveforms are shown in Figure 9b. The phase mismatch is almost rectified and the load current is exactly shared by the two DG units based on their power ratings in both pure resistive and inductive load conditions in Figure 9b.

In order to validate the harmonic sharing performance of the proposed method, a 3 kW nonlinear load is connected to the local AC bus. The nonlinear load is composed of a diode rectifier, line inductor, DC capacitor, and resistive load. The load sharing performance is compared in Figure 10. It has been demonstrated in previous studies that the harmonic sharing performance can be improved using the virtual output impedance [7,9,15]. Using the proposed method, since the output inductance is dynamically adjusted by the reactive power control, the effective power control bandwidth becomes wider. Consequently, the harmonic sharing performance is significantly enhanced using the proposed active impedance control scheme in Figure 6b.

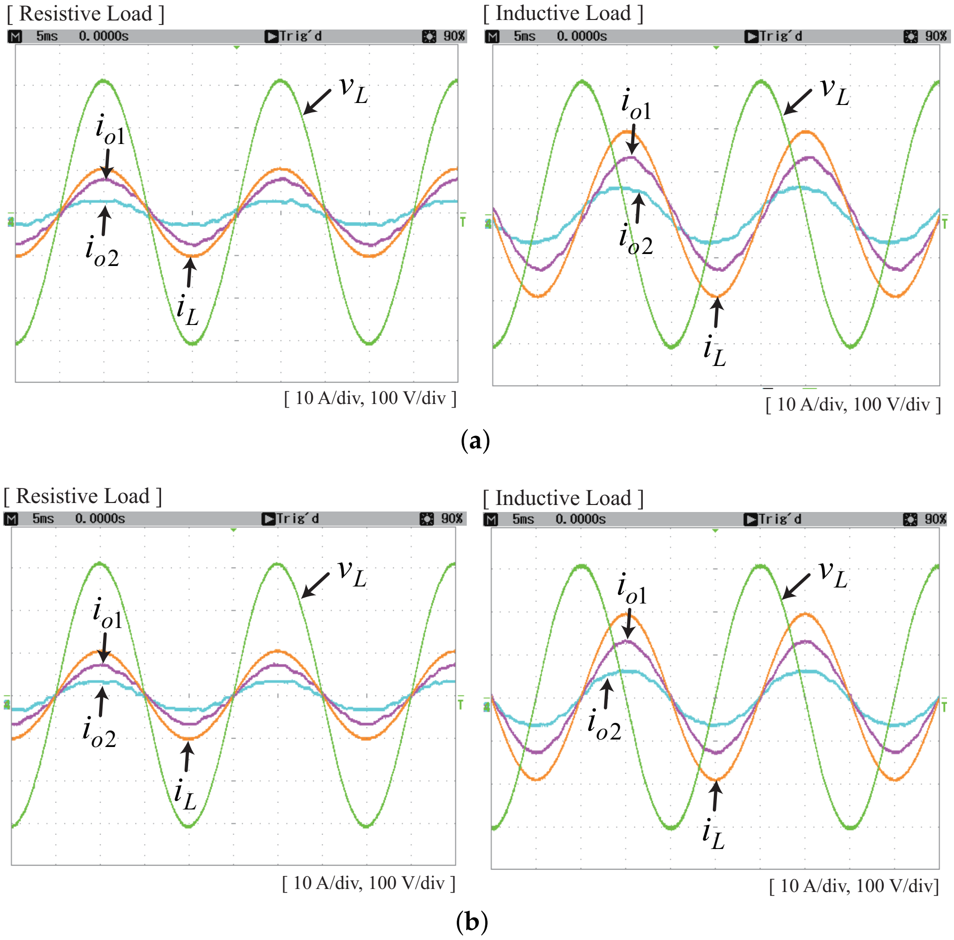

Figure 9. Controlled local AC bus voltage and output current waveforms in a resistive and inductive load condition: (**a**) conventional droop method; (**b**) proposed active impedance control.

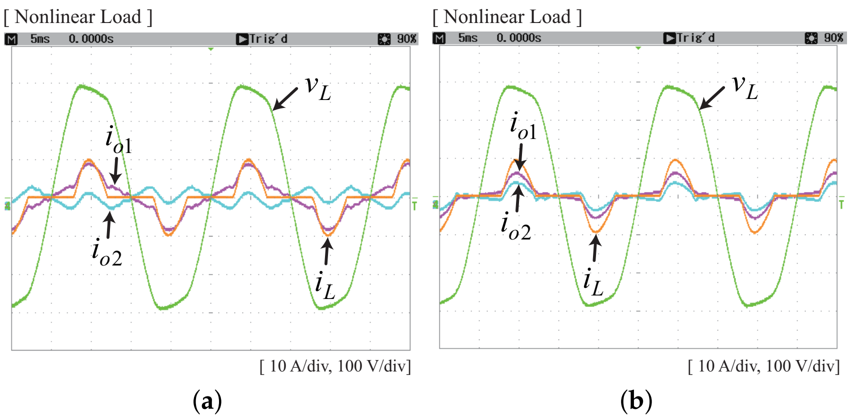

Figure 10. Controlled local AC bus voltage and output current waveforms in a nonlinear load condition: (**a**) conventional droop method; (**b**) proposed active impedance control.

The controlled power and load current waveforms are compared in Figure 11. A 5 kW pure resistive load is applied at the start and a 5 kVar inductive load is added abruptly. More than 700 W of circulating reactive power is observed in the pure resistive load condition in Figure 11a. The reactive power is transmitted from DG unit 1 to DG unit 2. However, the circulating reactive power almost disappears with the proposed method in Figure 11b. Moreover, it is observed that both real and reactive power sharing accuracies are improved in Figure 11b.

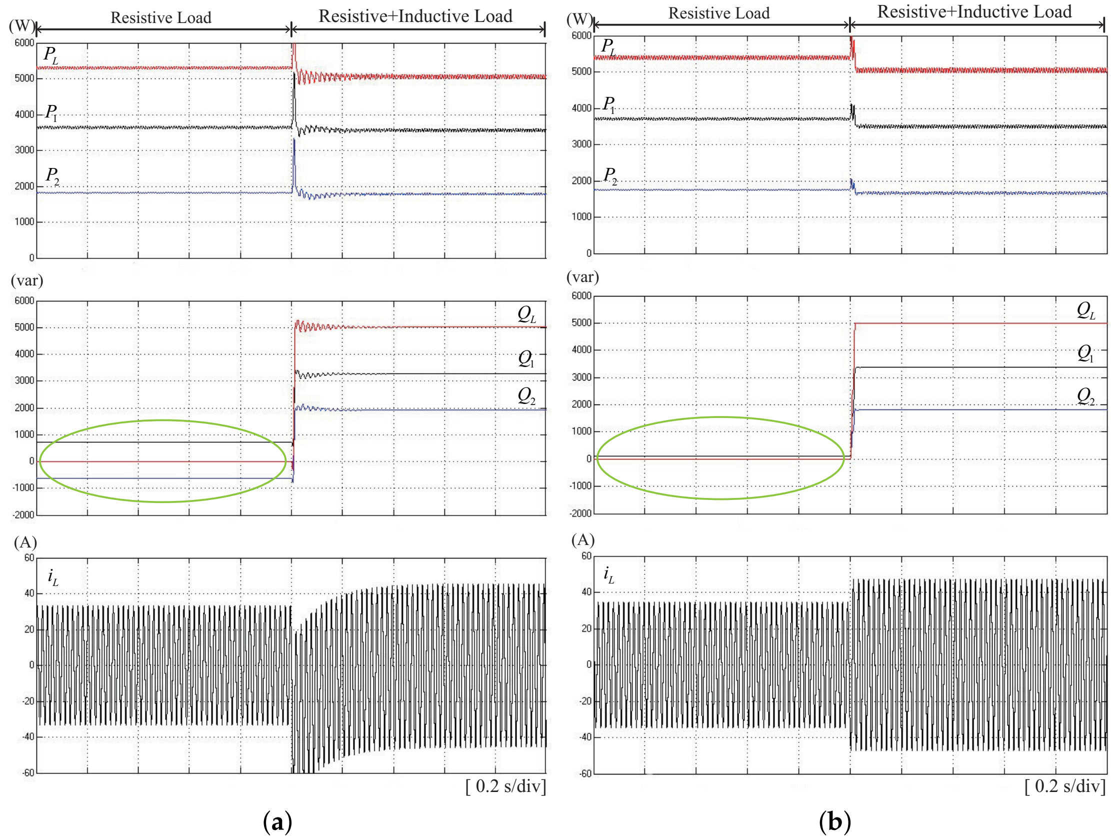

Figure 11. Power and current waveforms at the step load change: (**a**) conventional droop method; (**b**) proposed active impedance control.

5. Conclusions

An active output impedance control method for parallel connected grid-forming DG units is introduced in this paper. The proposed method utilizes the adjustable virtual output impedance for the parallel operation of voltage-controlled DG units. It is shown that the proposed method not only improves the power sharing accuracy but also minimizes the circulating current between the DG units. Therefore, it demonstrates a much better dynamic performance as compared to the conventional droop method. The effectiveness of the proposed method was validated using high-speed FPGA-based real-time HIL test results.

Acknowledgments: This study was supported by research funding from Chosun University, Gwangju, Republic of Korea, 2013.

Author Contributions: Jaehong Kim designed and performed the experiments; Younok Choi analyzed the experimental data; and Younok Choi and Jaehong Kim wrote the paper.

Conflicts of Interest: The authors declare no conflict of interest.

Nomenclature

DG	Distributed generator
PCC	Point of common coupling
FPGA	Field programmable gate array
HIL	Hardware-in-the-loop
DER	Distributed energy resource
STS	Static transfer switch
PLL	Phase-locked-loop

EPS	Electrical power system
PWM	Pulse-width-modulation
r_{ox}	Line resistance of DG unit x (Ω)
L_{ox}	Line inductance of DG unit x (H)
L_{fx}	Filter inductance of DG unit x (H)
r_{Lx}	Equivalent series resistance in the filter inductor of DG unit x (Ω)
C_{fx}	Filter capacitance of DG unit x (F)
r_{Cx}	Equivalent series resistance in the filter capacitor of DG unit x (Ω)
v_{ox}	LC filter output voltage of DG unit x (V)
i_{ox}	LC filter output current of DG unit x (V)
Z_{ox}	Internal impedance of DG unit x (Ω)
v_x	LC filter output voltage of DG unit x with virtual output impedance (V)
Z_x	Output impedance of DG unit x seen from local AC bus (Ω)
S_x	Output apparent power of DG unit x (VA)
P_x	Output real power of DG unit x (W)
$\bar{P}_x$	Nominal real power rating of DG unit x (W)
Q_x	Output reactive power of DG unit x (Var)
$\bar{Q}_x$	Nominal reactive power rating of DG unit x (Var)
θ_{xL}	Phase angle difference between DG unit x output voltage and local AC bus voltage (rad)
θ_{xy}	Phase angle difference between DG unit x output voltage and DG unit y output voltage (rad)
Z_{xy}	Intermediate impedance between DG unit x and DG unit y (Ω)
L_{xy}	Intermediate inductance between DG unit x and DG unit y (Ω)
P_{xy}	Real power flow from DG unit x to DG unit y (W)
Q_{xy}	Reactive power flow from DG unit x to DG unit y (Var)
Z_{vx}	Virtual output impedance of DG unit x (Ω)
L_{vx}	Virtual output inductance of DG unit x (H)
v_{vx}	Virtual voltage droop across the virtual output inductance of DG unit x (V)
V_n	Nominal magnitude of the grid voltage (V)
ω_v	Cut-off frequency of the virtual output inductance (rad/s)
ω_p	Cut-off frequency of the power measurement filter (rad/s)
ω_n	Nominal angular frequency of the grid voltage (rad/s)
f_n	Nominal frequency of the grid voltage (Hz)
L_n	Nominal output inductance (H)
D_{px}	P-ω droop gain in the conventional droop method
D_{qx}	Q-V droop gain in the conventional droop method
m_x	Effective droop gain in the proposed method
v_L	Load voltage in a local microgrid (V)
Z_L	Load impedance in a local microgrid (Ω)
S_L	Load apparent power (VA)
T_s	Sampling period in digital implementation
r_d	Virtual resistance in the active damping control
a_x	Power sharing ratio of DG unit x

References

1. Hou, X.; Sun, Y.; Yuan, W.; Han, H.; Zhong, C.; Guerrero, J.M. Conventional P-ω/Q-V droop control in highly resistive line of low-voltage converter-based AC microgrid. *Energies* **2016**, *9*, 943.
2. Garrasco, J.M.; Franquelo, L.G.; Bialasiewwicz, J.T.; Galvan, E.; Guisado, R.C.P.; Prats, M.A.M.; Leon, J.I.; Moreno-Alfonso, N. Power-electronic systems for the grid integration of renewable energy sources: A survey. *IEEE Trans. Ind. Electron.* **2006**, *53*, 1002–1016.
3. Zhong, Q.-C.; Weiss, G. Synchronverters: Inverters that mimic synchronous generators. *IEEE Trans. Ind. Electron.* **2011**, *58*, 1259–1267.
4. Li, Y.W.; Kao, C.N. An accurate power control strategy for power-electronics-interfaced distributed generation units operation in a low voltage multibus microgrid. *IEEE Trans. Power Electron.* **2009**, *24*, 2977–2988.

5. Chae, W.-K.; Won, J.-N.; Lee, H.-J.; Kim, J.-E.; Kim, J. Comparative analysis of voltage control in battery power converters for inverter-based AC microgrids. *Energies* **2016**, *9*, 596.
6. He, J.; Li, Y.W.; Guerrero, J.M.; Blaabjerg, F.; Vasquez, J.C. An islanding microgrid power sharing approach using enhanced virtual impedance control scheme. *IEEE Trans. Power Electron.* **2013**, *28*, 5272–5282.
7. Guerrero, J.M.; Vicuna, L.G.; Matas, J.; Castilla, M.; Miret, J. Output impedance design of parallel-connected UPS inverters with wireless load-sharing control. *IEEE Trans. Ind. Electron.* **2005**, *52*, 1126–1135.
8. Guerrero, J.M.; Hang, L.; Uceda, J. Control of distributed uninterruptible power supply systems. *IEEE Trans. Ind. Appl.* **2008**, *55*, 2845–2859.
9. Kim, J.; Guerrero, J.M.; Rodriguez, P.; Teodorescu, R.; Nam, K. Mode adaptive droop control with virtual output impedances for an inverter-based flexible AC microgrid. *IEEE Trans. Power Electron.* **2011**, *26*, 689–701.
10. He, J.; Li, Y.W.; Blaabjerg, F. An enhanced islanding microgrid reactive power, imbalance power, and harmonic power sharing scheme. *IEEE Trans. Power Electron.* **2015**, *30*, 3389–3401.
11. Lee, C.-T.; Chu, C.-C.; Cheng, P.-T. A new droop control method for the autonomous operation of distributed energy resource interface converters. *IEEE Trans. Power. Electron.* **2013**, *28*, 1980–1993.
12. Zhong, Q.-C. Harmonic droop controller to reduce the voltage harmonics of inverters. *IEEE Trans. Ind. Electron.* **2013**, *60*, 936–945.
13. Lee, T.-L.; Cheng, P.-T. Design of a new cooperative harmonic filtering strategy for distributed generation interface converters in an islanding network. *IEEE Trans. Power Electron.* **2007**, *22*, 1919–1927.
14. Brabandere, K.D.; Bolsens, B.; Keybus, J.V.D.; Woyte, A.; Driesen, J.; Belmans, R. A voltage and frequency droop control method for parallel inverters. *IEEE Trans. Power. Electron.* **2007**, *22*, 1107–1115.
15. He, J.; Li, Y.W. Analysis, design and implementation of virtual impedance for power electronics interfaced distributed generation. *IEEE Trans. Ind. Appl.* **2011**, *36*, 2525–2538.
16. Kim, J.; Hong, J.; Kim, H. Improved direct deadbeat voltage control with an actively damped inductor-capacitor plant model in an islanded AC microgrid. *Energies* **2016**, *9*, 978.
17. IEEE Standards Association. *IEEE Std. 1547. IEEE Standard for Interconnecting Distributed Resouces with Electric Power Systems*; IEEE Standards Association: Piscataway, NJ, USA, 2003.
18. IEEE Standards Association. *IEEE Std. 1547.4. IEEE Guide for Design, Operation, and Integration of Distributed Resource Island Systems with Electric Power Systems*; IEEE Standards Association: Piscataway, NJ, USA, 2011.
19. Liu, J.; Miura, Y.; Ise, T. Comparison of dynamic characteristics between virtual synchronous generator and droop control in inverter-based distributed generators. *IEEE Trans. Power Electron.* **2016**, *31*, 3600–3611.
20. Bergen, A.R.; Vittal, V. *Power Systems Analysis*, 2nd ed.; Prentice Hall: Upper Saddle River, NJ, USA, 2000; pp. 103–109.
21. Wang, X.; Blaabjerg, F.; Wu, W. Modeling and analysis of harmonic stability in an AC power-electronics-based power system. *IEEE Trans. Power Electron.* **2014**, *29*, 6421–6432.
22. Guerrero, J.M.; Vicuna, L.G.; Matas, J.; Castilla M.; Miret, J. A wireless controller to enhance dynamic performance of parallel inverters in distributed generation systems. *IEEE Trans. Power Electron.* **2004**, *19*, 1205–1213.
23. Li, Y.; Li, Y.W. Power management of inverter interfaced autonomous microgrid based on virtual frequency-voltage frame. *IEEE Trans. Smart Grid* **2011**, *2*, 30–40.
24. Kim, J.; Lee, J.; Nam, K. Inverter-based local AC bus votlage control utilizing two DOF control. *IEEE Trans. Power Electron.* **2008**, *23*, 1288–1298.
25. Merabet, A.; Ahmed, K.T.; Ibrahim, H.; Beguenane, R.; Chias, M.Y.M. Energy management and control system for laboratory scale microgrid based wind-PV-battery. *IEEE Trans. Sustain. Energy* **2017**, *8*, 145–154.